

2×10^{-13} Fractional Laser-Frequency Stability with a 7-cm Unequal-Arm Mach-Zehnder Interferometer

Victor Huarcaya^{ID},^{1,2} Miguel Dovale Álvarez^{ID},^{1,2,*} Daniel Penkert,^{1,2} Stefano Gozzo^{ID},^{1,2} Pablo Martínez Cano^{ID},^{1,2} Kohei Yamamoto,^{1,2} Juan José Esteban Delgado,^{1,2} Moritz Mehmet^{ID},^{1,2} Karsten Danzmann,^{1,2} and Gerhard Heinzel^{ID},^{1,2}

¹Max Planck Institute for Gravitational Physics (Albert Einstein Institute), Hannover D-30167, Germany

²Leibniz Universität Hannover, Hannover D-30167, Germany

(Received 23 June 2023; revised 1 August 2023; accepted 2 August 2023; published 31 August 2023)

To achieve subpicometer sensitivities in the millihertz band, laser interferometric inertial sensors rely on some form of reduction of the laser-frequency noise, typically by locking the laser to a stable frequency reference, such as the narrow-line-width resonance of an ultrastable optical cavity or an atomic or molecular transition. In this paper, we report on a compact laser-frequency stabilization technique based on an unequal-arm Mach-Zehnder interferometer that is subnanometer stable at 10 μHz , subpicometer at 0.5 mHz, and reaches a noise floor of $7 \text{ fm}/\sqrt{\text{Hz}}$ at 1 Hz. The interferometer is used in conjunction with a dc servo to stabilize the frequency of a laser down to a fractional instability below 4×10^{-13} at averaging times from 0.1 to 100 s. The technique offers a wide operating range, does not rely on complex lock-acquisition procedures, and can be readily integrated as part of the optical bench in future gravity missions.

DOI: 10.1103/PhysRevApplied.20.024078

I. INTRODUCTION

Laser interferometers are a key resource in many areas of science and technology, such as precision metrology, geodesy, and gravitational-wave detection. By measuring tiny distance variations with high precision, interferometers can be used to test fundamental physics [1] and reveal the gravity field of Earth [2,3] or the passing of gravitational waves [4–6].

Laser interferometers aiming to measure displacements with high precision suffer from laser-frequency noise coupling proportional to the optical-path-length mismatch Δl between the two interfering arms,

$$\frac{\delta l}{\Delta l} = \frac{\delta f}{f_0}, \quad (1)$$

where f_0 is the average frequency of the laser, δf is the laser-frequency noise, and δl is the resulting optical-path-length noise.

* miguel.dovale@aei.mpg.de

Published by the American Physical Society under the terms of the Creative Commons Attribution 4.0 International license. Further distribution of this work must maintain attribution to the author(s) and the published article's title, journal citation, and DOI. Open access publication funded by the Max Planck Society.

For example, the future space-based gravitational-wave detector *LISA* [7] aims to use laser interferometry to measure picometer-level changes in distance between spacecraft over a baseline of 2.5×10^6 km, which requires laser-frequency noise suppression by many orders of magnitude. Time-delay interferometry [8] is proposed to aid the task, setting a target on the laser-frequency prestabilization of [9]

$$\tilde{v} = 300 \frac{\text{Hz}}{\sqrt{\text{Hz}}} \left(\frac{1 \text{ m}}{\Delta L} \right) u(f) \quad (2)$$

for frequencies between 20 μHz and 1 Hz, where ΔL is the absolute ranging accuracy [10,11], currently estimated at 1 m, and $u(f)$ is the noise shape function, given by

$$u(f) = \sqrt{1 + \left(\frac{2 \text{ mHz}}{f} \right)^4}, \quad (3)$$

which describes a mixture of *white noise* with a flat power spectrum and *random-run* noise with a f^{-4} power spectrum.

The current baseline for LISA is using a cavity-stabilized laser similar to the one on board GRACE Follow-On [2,12,13] with a stability roughly an order of magnitude better than Eq. (2). Alternative schemes, such as arm locking [14–18] or stabilization to molecular iodine

hyperfine transitions near 532 nm [19,20], have been proposed. One such scheme involves prestabilizing the laser to an unequal-arm Mach-Zehnder interferometer (MZI), similar to the scheme used in the LISA technology package (LTP) interferometer [21,22] on board LISA Pathfinder [7,23–25].

Other prominent examples of laser interferometers at the frontier of physics are the gravitational-wave detectors *Advanced LIGO* [26] and *Advanced Virgo* [27], which are sensitive to displacements in the 20-Hz to 5-kHz band, reaching a noise floor of $2 \times 10^{-20} \text{ m}/\sqrt{\text{Hz}}$ at 100 Hz, 10 orders of magnitude below the level of ground motion at the site [28,29]. To achieve this amazing stability, seismic noise is reduced by a combination of passive and active stabilization stages [30]. The current schemes are limited by the readout noise of the sensors and lead to excess controls noise below 30 Hz [31]. New seismic isolation schemes [32–34] based on laser interferometric readout (see, e.g., Refs. [35–42]) promise to break the *seismic wall* and lead to sensitivity improvements of current and future detectors at the lower frequencies, with substantial rewards in astrophysical applications [43].

If not addressed, laser-frequency noise is one of the leading sources of noise in laser interferometric inertial sensors, particularly below 1 Hz, even if the macroscopic interferometer arm lengths are matched using best efforts and even when using commercial narrow laser linewidth (e.g., 1 kHz laser linewidth for 0.1 s averaging time). To achieve subpicometer sensitivities in the millihertz band, some form of reduction of the laser-frequency noise is required. The usual schemes involve stabilizing the laser to an ultrastable optical cavity or an atomic or molecular reference. Such schemes are also commercially available but they are bulky, costly, and rely on complex electronics.

In a previous paper [44], a compact quasimonolithic MZI with an intentional arm-length difference of 7 cm and a dc readout scheme has been introduced as a simpler alternative to conventional laser-locking schemes. In comparison to an optical cavity or an atomic or molecular reference, the MZI technique offers a wide operating range and does not require a complex lock-acquisition procedure. Continuous frequency tuning is possible by purely electronic means and does not require physically changing the resonance frequency of the frequency reference. The MZI in Ref. [44] has been shown to provide an impressive long-term dimensional stability, beating the subpicometer mark at 5 mHz. For comparison, the LTP interferometer beats this mark at 10 mHz [45].

In this paper, we present the next generation of this device, capable of reaching subpicometer sensitivity at 0.5 mHz. The combination of an ultrastable quasimonolithic fiber injector and a high-performance heat shield system allows us to realize a new benchmark of laser-frequency stability with a compact interferometer, yielding a

sensitivity improvement of one to nearly two orders of magnitude at low frequencies compared to the previous realization.

Employed in conjunction with an inertial sensor of matching stability, this method enables displacement sensing with a sensitivity better than $1 \text{ pm}/\sqrt{\text{Hz}} \times u(f)$ down to $10 \mu\text{Hz}$, which makes it a promising candidate for both ground-based seismic isolation systems or future gravity missions in space.

II. EXPERIMENTAL SETUP

The experimental setup is depicted in Fig. 1. A Mach-Zehnder interferometer with an arm-length difference of $\Delta l \approx 7 \text{ cm}$ is used as an ultrastable length reference for the laser-frequency stabilization of laser A, which is a 1064-nm nonplanar-ring-oscillator (NPRO) laser.

The design and construction of the MZI is described in Ref. [44] and a summary is given here. The MZI consists of a base plate made of CLEARCERAM™ CCX-HS ultrastable glass ceramic, to which fused-silica components are attached via UV-adhesive bonding. The base-plate material is chosen for its close to zero coefficient of thermal expansion around room temperature, while fused silica is the material of choice for the optical elements due to its excellent transmission properties. The base plate has dimensions of $13.5 \times 13.5 \times 3.6 \text{ cm}^3$.

The interferometer design was aided by the C++ optical modeling library IFOCAD [46]. In Ref. [44], an off-the-shelf commercial fiber coupler was used to inject laser light into the west port of the input beam splitter (BS1). In order to improve on the previously reported stability, especially at very long measurement times, a quasimonolithic fiber-injector optical subassembly (FIOS), developed in house, was retrofitted to the north port of BS1. The beam delivered by the FIOS is split into the short and long arms at BS1. The beam traveling along the long arm is reflected off mirrors M1 and M2 before being interfered with the short-arm beam at the recombination beam splitter BS2. Third and fourth beam splitters (BS3 and BS4) are placed in the north and east output ports of the beam combiner to allow the performance of diagnostic measurements, such as optical zero measurements, while maintaining symmetry between the photodetectors.

The precise positioning and orientation of components on the base plate are optimized via simulations to reduce the impact of spurious beams caused by residual reflections at the secondary surfaces, which have been identified as a critical source of noise in high-precision interferometers [47]. The input beam splitter and the beam combiner are wedged in order to separate the secondary reflections from the main optical path.

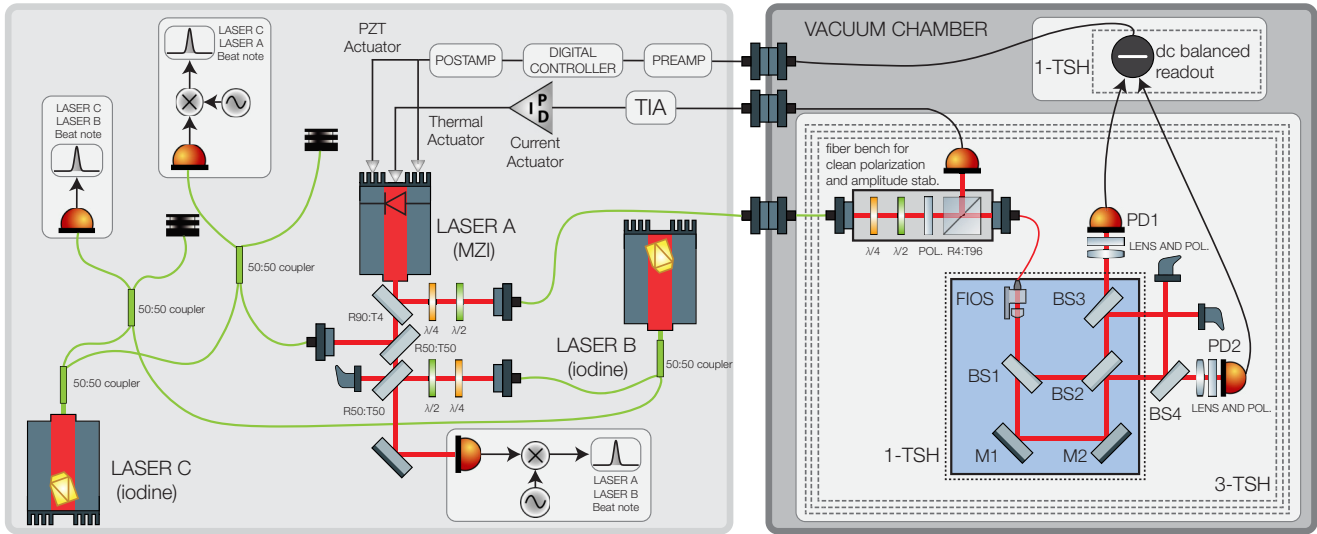


FIG. 1. The experimental setup. Light from laser A is injected into a vacuum chamber, where it is fed to the ultrastable interferometer (blue box) via a quasimonolithic fiber-injector optical subassembly (FIOS). The interferometer, along with the auxiliary optics and detectors for polarization cleaning, amplitude stabilization, and interferometric readout, is located inside a high-performance triple-layered thermal enclosure (3-TSH), with an additional single-layer thermal shield (1-TSH) surrounding just the Mach-Zehnder interferometer. The difference current between the two readout diodes is converted into a voltage by a homemade electronic circuit surrounded by yet another single-layer thermal enclosure (1-TSH). The signal is processed by a digital servo and fed back to the slow- and fast-frequency actuators of the laser. Laser A is beat with two iodine-stabilized lasers (lasers B and C) to help assess the achieved stability. The beat signals are mixed down to below 100 MHz with an ultrastable signal generator and read out via a phasemeter.

The FIOS [Fig. 2(a)] is made of six parts, combining a fiber end and a lens into a quasimonolithic nonadjustable package, thus significantly reducing the effects of both mechanical and thermal creep in comparison to conventional fiber injectors. The FIOS was first preassembled and then installed on the MZI with all other components already fixed to the base plate. The alignment of the FIOS was done with the help of a homemade positioning device and continuous contrast monitoring by applying a deep frequency modulation [48,49] to the laser. The final contrast achieved was 94% and no discernible contrast degradation was observed following a 2-year operational period encompassing several vacuum cycles, highlighting the satisfactory long-term stability of the UV-adhesive bonding.

The detection is performed by two identical 50 mm² circular active-area silicon *p-i-n* photodiodes located at the complementary output ports of BS2. A focusing lens is placed in front of each photodiode to help minimize transverse beam jitter and we incorporate thin-film polarizers with high extinction ratios mounted directly in front of the photodiodes to mitigate the impact of parasitic interferences arising from residual beams with orthogonal polarizations.

The photodiodes are operated in reverse bias voltage and connected in a balanced differential transimpedance amplifier (TIA) performing a dc subtraction. The basic schematic of the sensor is depicted in Fig. 3. The power

at each photodiode depends on the laser frequency f and is given by

$$\begin{aligned} P_1(f) &= p_1 \left[1 + c_1 \cos \left(\frac{2\pi f \Delta l}{c} + \varphi_0 \right) \right], \\ P_2(f) &= p_2 \left[1 - c_2 \cos \left(\frac{2\pi f \Delta l}{c} + \varphi_0 \right) \right], \end{aligned} \quad (4)$$

where $p_{1,2}$ are the optical powers at each photodetector in midfringe, $c_{1,2}$ are the interferometric contrasts at each photodetector, Δl is the optical-path-length difference of the interferometer, c is the speed of light, and φ_0 is an arbitrary constant. After the TIA, the resulting signal is given by

$$\begin{aligned} v(f) &= G [P_1(f) - P_2(f)], \\ &= G \left[p_1 - p_2 + (c_1 p_1 + c_2 p_2) \cos \left(\frac{2\pi f \Delta l}{c} + \varphi_0 \right) \right], \end{aligned} \quad (5)$$

where G [V/W] is the transimpedance gain. In order to attain balanced operation (i.e., $p_1 = p_2$), we leverage the reflectivity dependence of BS4 on the macroscopic beam incidence angle, achieving nearly equal power levels on both photodiodes, such that

$$v(f) = G p_1 (c_1 + c_2) \cos \left(\frac{2\pi f \Delta l}{c} + \varphi_0 \right). \quad (6)$$

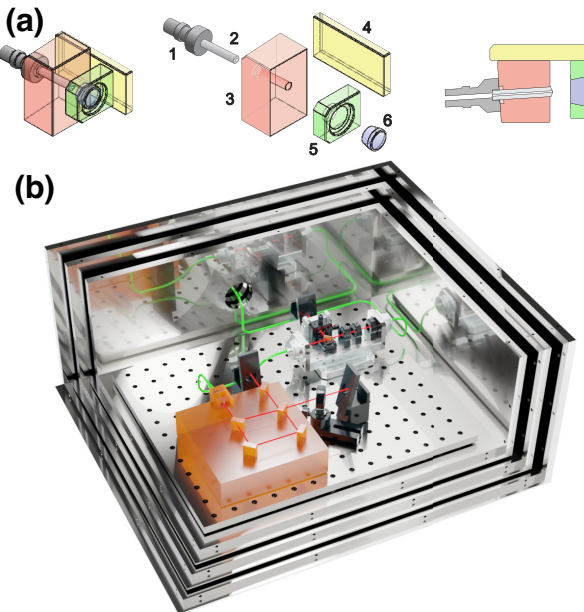


FIG. 2. The FIOS (a) consists of a polarization-maintaining 1064-nm single-mode optical fiber (1) equipped with a bare ferrule (2) held in place by a tightly fitted hole in the fused-silica fiber mount (3). An off-the-shelf antireflectively coated aspherical lens of D-ZLAF52LA glass, modified for a tapered outer surface (6), is UV glued into a matching hole in the fused-silica lens holder (5). Finally, the fiber mount and the lens holder are joined together at the desired distance, position, and orientation using a longitudinal girder of fused silica (4) and two thermally compensating layers of UV adhesive. The next-generation unequal-arm Mach-Zehnder interferometer (b) consists of an ultrastable glass ceramic base plate to which the fused-silica components and the FIOS are bonded via UV adhesive. A set of three aluminum heat shields isolates the interferometer from external temperature fluctuations. The aluminum-plate surfaces are polished to lower their emissivity and slow down radiative heat transfer inside the enclosure.

Equation (6) has periodic zero crossings that we use for laser locking. The slope of the error signal at the operating point is proportional to the available optical power, the interferometric contrasts, the transimpedance gain, and the arm-length difference of the interferometer.

A Moku:Lab by Liquid Instruments [50] is used as a digital controller to provide feedback based on the generated error signal to both the slow thermal actuator and the fast piezoelectric transducer actuator of the NPRO laser. Additionally, a preamplifier (SR560 by Stanford Research Systems) and a postamplifier equipped with a low-pass filter are used to mitigate analog-to-digital converter noise originating from the digital servo and to enhance the low-frequency gain, respectively.

When the laser is locked to the MZI, the optical-pathlength stability of the interferometer is transferred to the frequency stability of the laser, obeying Eq. (1). To isolate

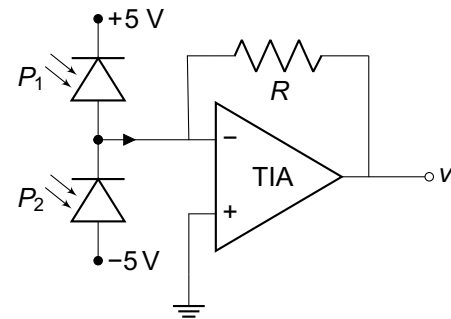


FIG. 3. A schematic of the balanced differential transimpedance amplifier (TIA).

the MZI from external perturbations affecting its path-length noise δl , it is placed inside a vacuum chamber at a moderate pressure of 10^{-6} mbar and surrounded by a set of three aluminum heat shields [Fig. 2(b)], similar to the systems designed for high-performance metrology with ultrastable optical reference cavities [51,52].

Each shield consists of six 10-mm aluminum plates fastened together via M4 screws and is supported by three 10-mm polyether ether ketone (PEEK) spheres that rest on 5-mm-deep conical cutouts made to each of the base plates, with the exception of the outermost shield, that rests on three PEEK semispheres placed on the surface of the vacuum chamber. The plates are polished to yield a low emissivity, thereby slowing radiative heat transfer inside the enclosure. The resulting system has an extremely slow response to temperature changes, with a thermal time constant of about a week that is largely dominated by a surface-to-surface radiative exchange.

Laser A is split two ways. One part of the light feeds the vacuum chamber, where it is further split such that a small fraction is captured by a photoreceiver for amplitude stabilization of the laser and the rest is injected into the MZI. The other part is split two ways and interfered with two reference lasers to enable measurements of the achieved stability. The reference systems, lasers B and C, are two iodine-stabilized NPRO lasers (Prometheus by Coherent), locked to the molecular iodine hyperfine transitions R(56)32-0 “a1” and “a2.” The two reference lasers are also interfered, generating a third beat-note signal that allows us to perform a complete characterization of the stability of the three systems. The three beat notes are captured by high-speed InGaAs photoreceivers. The two beat notes with laser A, which are in the (0.5–2)-GHz band, are mixed down to less than 100 MHz using an ultrastable gigahertz signal generator (SMB100A by Rohde & Schwarz). Finally, the three beat notes are tracked simultaneously by a Moku:Pro phasemeter [50]. The noise contributions of the R&S SMB100A and the phasemeter instrument are measured to be well below 1 Hz/ $\sqrt{\text{Hz}}$ throughout the whole band.

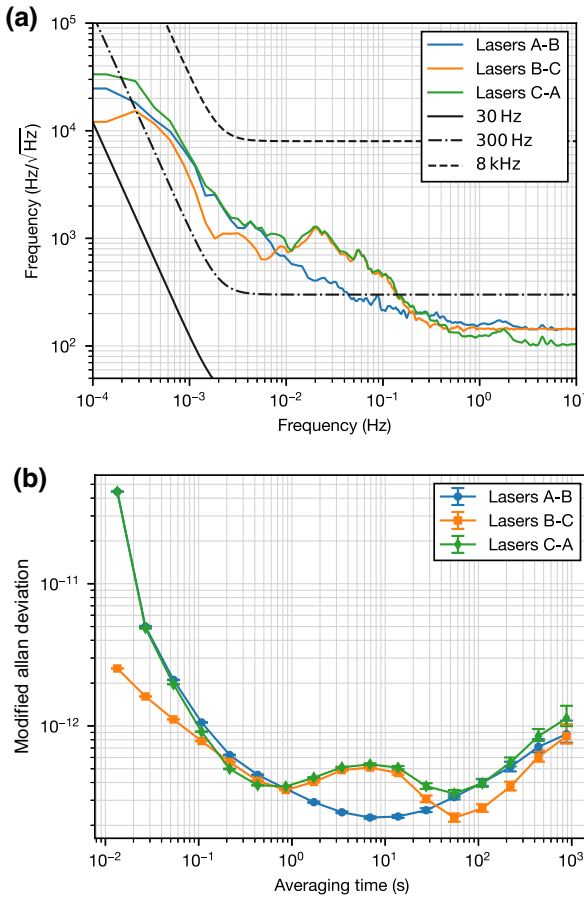


FIG. 4. The frequency spectral densities (a) and modified Allan deviations (b) of a 2-h measurement of the three beat notes (A, MZI-stabilized laser; B, C, iodine-stabilized lasers). Also shown are the frequency noise spectral densities of $30 \text{ Hz}/\sqrt{\text{Hz}} \times u(f)$, $300 \text{ Hz}/\sqrt{\text{Hz}} \times u(f)$ and $8 \text{ kHz}/\sqrt{\text{Hz}} \times u(f)$.

III. RESULTS

The frequency spectral densities [53] and modified Allan deviations [54] of the three beat notes are shown in Figs. 4(a) and 4(b), respectively, for a typical 2-h measurement at a rate of 150 samples/s. Also shown in Fig. 4(a) are the frequency noise spectral densities of $30 \text{ Hz}/\sqrt{\text{Hz}}$, $300 \text{ Hz}/\sqrt{\text{Hz}}$, and $8 \text{ kHz}/\sqrt{\text{Hz}}$, scaled by Eq. (3), respectively, representing the stability of a space-qualified cavity-stabilized laser system, the LISA laser-frequency-prestabilization target, and the picometer-equivalent frequency instability of an interferometer with 7-cm arm-length difference [see Eq. (1)].

Inspection of any of these two plots, containing largely the same information, reveals that the MZI-stabilized system (laser A) offers a stability comparable to that of the two iodine-stabilized systems (lasers B and C). This complicates the assessment of the achieved stability, since the frequency noise of the reference lasers cannot be neglected in comparison to the frequency noise of the unit under test.

A bump in the noise of the B-C and the C-A beat notes is evident in both the amplitude-spectral-density estimates and the modified Allan deviations. The bump can be seen at frequencies between 100 mHz and 0.2 Hz or at averaging times between 2 and 50 s. From this analysis, it is not clear which of lasers A or C is responsible for the noise degradation.

To evaluate the performance of each single laser, independently from the rest, we carry out a three-cornered-hat analysis [55] using the modified Allan deviation (MDEV) and the Hadamard deviation (HDEV) as the statistical functions of choice [54].

The MDEV is chosen for its ability to distinguish between white and flicker phase noise at short averaging times (i.e., at short $\tau = m\tau_0$, where τ is the averaging time, τ_0 is the gate time or sampling time, and m is the averaging factor) or, equivalently, at high frequencies. The MDEV is also widely used in the time and frequency standards community, such that our stability results may be easily compared to other references.

The HDEV is chosen for its ability to handle divergent noise sources at long averaging times. The MDEV is not a good statistic for processes having power spectral densities with a f^{-4} dependency [e.g., as in Eq. (3)], as the obtained variance at long τ may depend on the measurement time. On the other hand, the HDEV examines the second difference of the fractional frequencies, which makes it robust against f^{-4} noise, allowing a direct comparison of the achieved long-term stability with noise allocations following Eq. (3).

Frequency data were taken over 12 h by the same phasemeter with a gate time of 6.7 ms. The data set was cut into ten sections of 1.2 h, a linear drift was removed for compensating the temperature drift in each section, and the individual Allan deviations were calculated. The arithmetic mean and standard deviation of the resulting modified Allan deviation are shown in Fig. 5, which also shows the MDEV of the MZI stability reported in Ref. [44], obtained via a domain conversion from the power spectral density using the MDEV transfer function [56], and the MDEV of virtual beat notes having white frequency noise spectral densities at the $30 \text{ Hz}/\sqrt{\text{Hz}}$, $300 \text{ Hz}/\sqrt{\text{Hz}}$, and $8 \text{ kHz}/\sqrt{\text{Hz}}$ levels.

Finally, given that we are only interested in the Hadamard deviation at long averaging times, the data are down-sampled by a factor of 100 in order to decrease the otherwise long computation time of the HDEV. To down-sample the data, an averaging operation is performed, which limits the results to $\tau > 100\tau_0$. The results are shown in Fig. 6, together with the HDEV corresponding to virtual beat notes with frequency spectral densities of $30 \text{ Hz}/\sqrt{\text{Hz}} \times u(f)$, $300 \text{ Hz}/\sqrt{\text{Hz}} \times u(f)$, and $8 \text{ kHz}/\sqrt{\text{Hz}} \times u(f)$, obtained by numerically computing the HDEV on data generated by a simple noise model that conforms to Eq. (3).

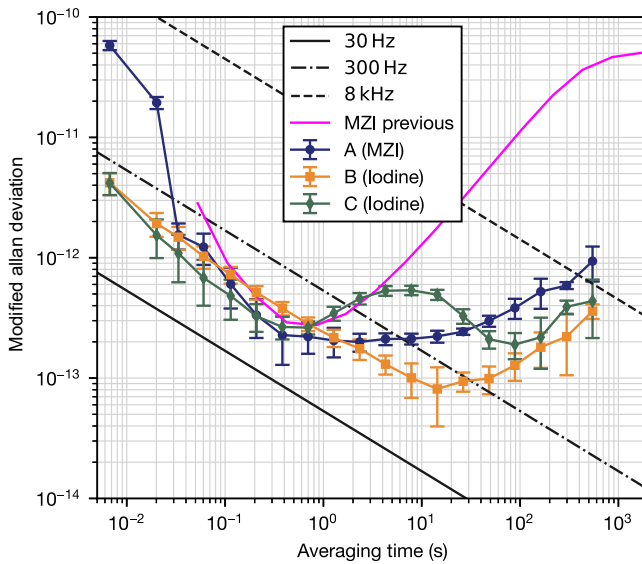


FIG. 5. The modified Allan deviation of the three stabilized lasers derived from a three-cornered-hat analysis. The data show the average instability of ten data sets with a duration of 1.2 h each. The error bars represent the standard deviation of the data averaged for each point. Also shown are the modified Allan deviations of virtual beat notes with white frequency noise at $30 \text{ Hz}/\sqrt{\text{Hz}}$, $300 \text{ Hz}/\sqrt{\text{Hz}}$, and $8 \text{ kHz}/\sqrt{\text{Hz}}$.

The three-cornered-hat analysis reveals the individual performance of each laser. The noise bump of laser C is successfully isolated at τ between 1 and 10 s. At $\tau > 10$

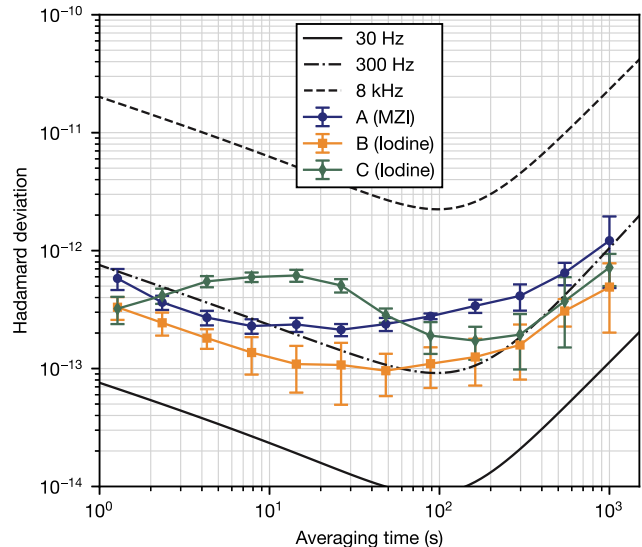


FIG. 6. The Hadamard deviation of the three stabilized lasers derived from a three-cornered-hat analysis. The data show the average instability of 10 data sets with a duration of 1.2 h each. The error bars represent the standard deviation of the data averaged for each point. Also shown are the Hadamard deviations corresponding to virtual beat notes having frequency spectral densities of $30 \text{ Hz}/\sqrt{\text{Hz}} \times u(f)$, $300 \text{ Hz}/\sqrt{\text{Hz}} \times u(f)$, and $8 \text{ kHz}/\sqrt{\text{Hz}} \times u(f)$.

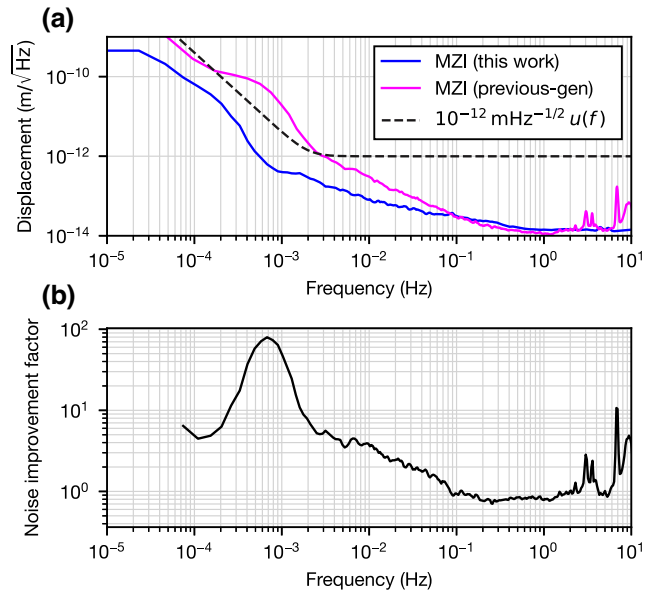


FIG. 7. The spectral density of the optical-path-length noise in the MZI from a 12-h measurement, as probed by laser B (a). The noise floor is limited at the lower frequencies by temperature fluctuations coupling as interferometer path-length changes. At frequencies higher than 1 mHz, a $1/f$ power spectrum is observed, which is suspected to be due to the effect of thermal drifts in the sensitive transimpedance amplifier used to convert the differential interferometric current into a voltage for laser locking. Also shown are the previously realized stability and the $1 \text{ pm}/\sqrt{\text{Hz}} \times u(f)$ displacement-noise allocation commonly used for the local interferometry in LISA. The ratio between the spectral densities of the two measurements yields the noise improvement factor (b), showing a factor 80 improvement at 0.7 mHz.

s, laser B is roughly a factor of 2–3 more stable than laser A. At lower averaging times, their stability is very similar, except at very short averaging times ($\tau \sim 10$ ms), where the MZI suffers from short-lived instabilities originating from the coupling of vibrations of the vacuum pumps.

As per the obtained MDEV, the fractional frequency instability of the MZI is below 10^{-12} at averaging times greater than 0.1 s and in excess of a few hundred seconds. A maximal stability of 2×10^{-13} is achieved between 1 and 10 s that is dominated by flicker-frequency noise (i.e., $1/f$ noise). In this range, the MZI is compatible with the LISA frequency-prestabilization target [Eq. (2)]. On the other hand, the HDEV analysis reveals that the MZI does not meet the LISA target at averaging times between 10 s and a few hundred seconds (e.g., it is a factor of 2 less stable at 50 s). At 1000 s, the MZI stability is close to the target, hinting that at even longer measurement times, the system may be compliant with this noise allocation, which can only be revealed by performing longer measurements.

Using Eq. (1), we can infer the achieved MZI path-length stability as probed by laser B, shown in Fig. 7,

and compare it against the previous results [44]. Thanks to the three-cornered-hat analysis, we have confidence in the estimated stability at the lower frequencies, e.g., at frequencies below 100 mHz, where it has been shown that laser B is, on average, 2.4 times more stable than laser A. At higher frequencies (e.g., around 1 Hz), the stabilities of the three lasers are similar, so the performance of laser A may be estimated as 1/2 of the stability of the A-B or C-A beat notes, which yields a noise floor of 7 fm/√Hz at 1 Hz. These results showcase a clear performance improvement of the setup below 100 mHz.

IV. CONCLUSIONS

An ultrastable Mach-Zehnder interferometer with unequal arm lengths capable of reaching 1 pm/√Hz × $u(f)$ from 10 μHz to 10 Hz has been presented. The new system is one to two orders of magnitude more stable in the lower frequencies than the previous realization. This stability has been achieved by applying a combination of two passive techniques for reducing noise sources of thermal origin. First, a quasimonolithic fiber injector made of fused-silica components provides an ultrastable input beam that is much more robust to temperature changes than is possible with conventional fiber injectors. Second, a high-performance enclosure provides an ultraquiet thermal environment, reducing the coupling of temperature-driven effects to path-length noise in the interferometer, such as thermoelastic deformation of the base plate and components, and refractive-index fluctuations.

A combination of frequency and time-domain analysis techniques has been used to assess the stability of the MZI-stabilized laser along with two iodine-stabilized reference lasers. The individual stability of each system has been disentangled from a simultaneous three-signal measurement using the three-cornered-hat method. Due to the nature of the involved noise sources, which are white frequency noise at high frequency (i.e., at a short averaging time, τ) and random-run noise at low frequency (i.e., at long τ), two different variance functions have been used, with one providing greater confidence at short τ (the modified Allan deviation) and the other greater confidence at long τ (the Hadamard deviation).

The three-cornered-hat analyses reveal that the stability of the MZI system is comparable to that of the two reference systems, which are based on stabilization to molecular iodine hyperfine transitions near 532 nm [57]. The frequency of our MZI-stabilized laser is within the target of 300 Hz/√Hz × $u(f)$ for all frequencies above 40 mHz. At frequencies between 10 μHz and 40 mHz, it is a factor of 1–5 less stable. The stability could be improved by increasing the arm-length difference of the interferometer (e.g., from 7 cm to 40 cm, as in the LTP interferometer) and addressing the associated complexities of the longer optical path length. However, a more exciting prospect is to

combine the techniques of Mach-Zehnder stabilization and arm locking [9], which could lead to a frequency stability orders of magnitude better than 300 Hz/√Hz × $u(f)$, potentially allowing the requirements on time-delay interferometry to be relaxed. Since the reference interferometer can be integrated as part of the optical bench that is already a central feature in this type of mission, this technique eliminates the need for a separate laser-stabilization subsystem, which makes this an interesting scheme for future gravity missions [58,59].

ACKNOWLEDGMENTS

We would like to thank Germán Fernández Barranco for his help with analog electronics and Oliver Gerberding and Katharina-Sophie Isleif for their continued cooperation in the project. M.D.A. would like to thank Olaf Hartwig for fruitful discussions on time-domain stability analysis. This work was funded by the Deutsche Forschungsgemeinschaft (DFG, German Research Foundation) Project-ID 434617780-SFB 1464. We acknowledge support from the DFG Sonderforschungsbereich 1128 Relativistic Geodesy and Cluster of Excellence “QuantumFrontiers: Light and Matter at the Quantum Frontier: Foundations and Applications in Metrology” (EXC-2123, Project No. 390837967) and the Max Planck Society (MPS) through the LEGACY cooperation on low-frequency gravitational-wave astronomy (M.IF.A.QOP18098). We also acknowledge support by the German Aerospace Center (DLR) with funds from the Federal Ministry of Economics and Technology (BMWi), according to a decision of the German Federal Parliament (Grant No. 50OQ2301, based on Grants No. 50OQ0601, No. 50OQ1301, and No. 50OQ1801).

-
- [1] H. Müller, S. Herrmann, C. Braxmaier, S. Schiller, and A. Peters, Modern Michelson-Morley Experiment Using Cryogenic Optical Resonators, *Phys. Rev. Lett.* **91**, 020401 (2003).
 - [2] R. P. Kornfeld, B. W. Arnold, M. A. Gross, N. T. Dahya, W. M. Klipstein, P. F. Gath, and S. Bettadpur, GRACE-FO: The gravity recovery and climate experiment follow-on mission, *J. Spacecr. Rockets* **56**, 931 (2019).
 - [3] B. D. Tapley *et al.*, Contributions of GRACE to understanding climate change, *Nat. Clim. Chang.* **9**, 358 (2019).
 - [4] B. P. Abbott, R. Abbott, T. D. Abbott, M. R. Abernathy, F. Acernese, K. Ackley, C. Adams, T. Adams, P. Addesso, and R. X. Adhikari *et al.*, (LIGO Scientific Collaboration and Virgo Collaboration), Observation of Gravitational Waves from a Binary Black Hole Merger, *Phys. Rev. Lett.* **116**, 061102 (2016).
 - [5] B. P. Abbott, R. Abbott, T. D. Abbott, F. Acernese, K. Ackley, C. Adams, T. Adams, P. Addesso, R. X. Adhikari, and V. B. Adya *et al.*, (LIGO Scientific Collaboration and Virgo Collaboration), Gw170817: Observation of Gravitational

- Waves from a Binary Neutron Star Inspiral, *Phys. Rev. Lett.* **119**, 161101 (2017).
- [6] M. C. Miller and N. Yunes, The new frontier of gravitational waves, *Nature* **568**, 469 (2019).
- [7] Karsten Danzmann, for the LISA Pathfinder Team and the eLISA Consortium, LISA and its pathfinder, *Nat. Phys.* **11**, 613 (2015).
- [8] M. Tinto, D. A. Shaddock, J. Sylvestre, and J. W. Armstrong, Implementation of time-delay interferometry for LISA, *Phys. Rev. D* **67**, 122003 (2003).
- [9] LISA Frequency control study team, LISA Frequency Control White Paper, LISA-JPL-TN-823 (2000).
- [10] J. J. Esteban, A. F. García, S. Barke, A. M. Peinado, F. G. Cervantes, I. Bykov, G. Heinzel, and K. Danzmann, Experimental demonstration of weak-light laser ranging and data communication for LISA, *Opt. Express* **19**, 15937 (2011).
- [11] A. J. Sutton, K. McKenzie, B. Ware, G. de Vine, R. E. Spero, W. Klipstein, and D. A. Shaddock, Improved optical ranging for space based gravitational wave detection, *Classical Quantum Gravity* **30**, 075008 (2013).
- [12] R. Pierce, M. Stephens, P. Kaptchen, J. Leitch, D. Bender, W. M. Folkner, W. M. Klipstein, D. Shaddock, R. Spero, R. Thompson, N. Yu, and M. Watkins, in *Conference on Lasers and Electro-Optics 2012* (OSA, San Jose, California, USA, 2012).
- [13] K. Abich *et al.*, In-Orbit Performance of the GRACE Follow-On Laser Ranging Interferometer, *Phys. Rev. Lett.* **123**, 031101 (2019).
- [14] B. S. Sheard, M. B. Gray, D. E. McClelland, and D. A. Shaddock, Laser frequency stabilization by locking to a LISA arm, *Phys. Lett. A* **320**, 9 (2003).
- [15] J. Thorpe and G. Mueller, Experimental verification of arm-locking for LISA using electronic phase delay, *Phys. Lett. A* **342**, 199 (2005).
- [16] B. S. Sheard, M. B. Gray, and D. E. McClelland, High-bandwidth laser frequency stabilization to a fiber-optic delay line, *Appl. Opt.* **45**, 8491 (2006).
- [17] V. Wand, Y. Yu, S. Mitryk, D. Sweeney, A. Preston, D. Tanner, G. Mueller, J. I. Thorpe, and J. Livas, Implementation of armlocking with a delay of 1 s in the presence of Doppler shifts, *J. Phys.: Conf. Ser.* **154**, 012024 (2009).
- [18] J. T. Valliyakalayil, A. J. Sutton, R. E. Spero, D. A. Shaddock, and K. McKenzie, Enhanced frequency noise suppression for LISA by combining cavity and arm locking control systems, *Phys. Rev. D* **105**, 062005 (2022).
- [19] V. Leonhardt and J. B. Camp, Space interferometry application of laser frequency stabilization with molecular iodine, *Appl. Opt.* **45**, 4142 (2006).
- [20] T. Schuldt, K. Döringshoff, M. Oswald, E. V. Kovalchuk, A. Peters, and C. Braxmaier, Absolute laser frequency stabilization for LISA, *Int. J. Mod. Phys. D* **28**, 1845002 (2019).
- [21] G. Heinzel, C. Braxmaier, R. Schilling, A. R. diger, D. Robertson, M. te Plate, V. Wand, K. Arai, U. Johann, and K. Danzmann, Interferometry for the LISA technology package (LTP) aboard SMART-2, *Classical Quantum Gravity* **20**, S153 (2003).
- [22] G. Heinzel, V. Wand, A. García, O. Jennrich, C. Braxmaier, D. Robertson, K. Middleton, D. Hoyland, A. Rüdiger, R. Schilling, U. Johann, and K. Danzmann, The LTP interferometer and phasemeter, *Classical Quantum Gravity* **21**, S581 (2004).
- [23] M. Armano *et al.*, Sub-Femto-g Free Fall for Space-Based Gravitational Wave Observatories: LISA Pathfinder Results, *Phys. Rev. Lett.* **116**, 231101 (2016).
- [24] M. Armano *et al.*, Beyond the Required LISA Free-Fall Performance: New LISA Pathfinder Results down to 20 μ Hz, *Phys. Rev. Lett.* **120**, 061101 (2018).
- [25] M. Armano *et al.*, (LISA Pathfinder Collaboration), LISA Pathfinder platform stability and drag-free performance, *Phys. Rev. D* **99**, 082001 (2019).
- [26] L. S. Collaboration, Advanced LIGO, *Classical Quantum Gravity* **32**, 074001 (2015).
- [27] F. Acernese *et al.*, Advanced Virgo: A second-generation interferometric gravitational wave detector, *Classical Quantum Gravity* **32**, 024001 (2014).
- [28] D. V. Martynov, E. D. Hall, B. P. Abbott, R. Abbott, T. D. Abbott, C. Adams, R. X. Adhikari, R. A. Anderson, S. B. Anderson, and K. Arai *et al.*, Sensitivity of the advanced LIGO detectors at the beginning of gravitational wave astronomy, *Phys. Rev. D* **93**, 112004 (2016).
- [29] A. Buikema, C. Cahillane, G. Mansell, C. Blair, R. Abbott, C. Adams, R. Adhikari, A. Ananyeva, S. Appert, and K. Arai *et al.*, Sensitivity and performance of the advanced LIGO detectors in the third observing run, *Phys. Rev. D* **102**, 062003 (2020).
- [30] L. Carbone, S. M. Aston, R. M. Cutler, A. Freise, J. Greenhalgh, J. Heefner, D. Hoyland, N. A. Lockerbie, D. Lodhia, N. A. Robertson, C. C. Speake, K. A. Strain, and A. Vecchio, Sensors and actuators for the advanced LIGO mirror suspensions, *Classical Quantum Gravity* **29**, 115005 (2012).
- [31] C. Cahillane and G. Mansell, Review of the advanced LIGO gravitational wave observatories leading to observing run four, *Galaxies* **10**, 36 (2022).
- [32] C. M. Mow-Lowry and D. Martynov, A 6D interferometric inertial isolation system, *Classical Quantum Gravity* **36**, 245006 (2019).
- [33] A. S. Ubhi, J. Smetana, T. Zhang, S. Cooper, L. Prokhorov, J. Bryant, D. Hoyland, H. Miao, and D. Martynov, A six degree-of-freedom fused silica seismometer: Design and tests of a metal prototype, *Classical Quantum Gravity* **39**, 015006 (2021).
- [34] J. van Dongen, L. Prokhorov, S. J. Cooper, M. A. Barton, E. Bonilla, K. L. Dooley, J. C. Driggers, A. Effler, N. A. Holland, A. Huddart, M. Kasprzack, J. S. Kissel, B. Lantz, A. L. Mitchell, J. O'Dell, A. Pele, C. Robertson, and C. M. Mow-Lowry, Reducing control noise in gravitational wave detectors with interferometric local damping of suspended optics, *Rev. Sci. Instrum.* **94**, 054501 (2023).
- [35] S. J. Cooper, C. J. Collins, A. C. Green, D. Hoyland, C. C. Speake, A. Freise, and C. M. Mow-Lowry, A compact, large-range interferometer for precision measurement and inertial sensing, *Classical Quantum Gravity* **35**, 095007 (2018).
- [36] K.-S. Isleif, G. Heinzel, M. Mehmet, and O. Gerberding, Compact Multifringe Interferometry with Subpicometer Precision, *Phys. Rev. Appl.* **12**, 034025 (2019).
- [37] Y. Yang, K. Yamamoto, V. Huarcaya, C. Vorndamme, D. Penkert, G. F. Barranco, T. S. Schwarze, M. Mehmet, J. J.

- E. Delgado, J. Jia, G. Heinzel, and M. D. Álvarez, Single-element dual-interferometer for precision inertial sensing, *Sensors* **20**, 4986 (2020).
- [38] Y. Zhang and F. Guzman, Quasi-monolithic heterodyne laser interferometer for inertial sensing, *Opt. Lett.* **47**, 5120 (2022).
- [39] Y. Zhang and F. Guzman, Fiber-based two-wavelength heterodyne laser interferometer, *Opt. Express* **30**, 37993 (2022).
- [40] S. L. Kranzhoff, J. Lehmann, R. Kirchhoff, M. Carlassara, S. J. Cooper, P. Koch, S. Leavey, H. Lück, C. M. Mow-Lowry, J. Wöhler, J. von Wrangel, and D. S. Wu, A vertical inertial sensor with interferometric readout, *Classical Quantum Gravity* **40**, 015007 (2022).
- [41] J. Smetana, R. Walters, S. Bauchinger, A. S. Ubhi, S. Cooper, D. Hoyland, R. Abbott, C. Baune, P. Fritchel, O. Gerberding, S. Köhnke, H. Miao, S. Rode, and D. Martynov, Compact Michelson Interferometers with Subpicometer Sensitivity, *Phys. Rev. Appl.* **18**, 034040 (2022).
- [42] H. Yan, H.-C. Yeh, and Q. Mao, High precision six-degree-of-freedom interferometer for test mass readout, *Classical Quantum Gravity* **39**, 075024 (2022).
- [43] H. Yu, D. Martynov, S. Vitale, M. Evans, D. Shoemaker, B. Barr, G. Hammond, S. Hild, J. Hough, S. Huttner, S. Rowan, B. Sorazu, L. Carbone, A. Freise, C. Mow-Lowry, K. L. Dooley, P. Fulda, H. Grote, and D. Sigg, Prospects for Detecting Gravitational Waves at 5 Hz with Ground-Based Detectors, *Phys. Rev. Lett.* **120**, 141102 (2018).
- [44] O. Gerberding, K.-S. Isleif, M. Mehmet, K. Danzmann, and G. Heinzel, Laser-Frequency Stabilization via a Quasi-monolithic Mach-Zehnder Interferometer with Arms of Unequal Length and Balanced dc Readout, *Phys. Rev. Appl.* **7**, 024027 (2017).
- [45] M. Armano *et al.*, Sensor Noise in LISA Pathfinder: In-Flight Performance of the Optical Test Mass Readout, *Phys. Rev. Lett.* **126**, 131103 (2021).
- [46] IfoCAD, <http://www.lisa.aei-hannover.de/ifocad/>.
- [47] K.-S. Isleif, *Laser Interferometry for LISA and Satellite Geodesy Missions* (Institutional Repository of Leibniz Universität Hannover, Hannover, Germany, 2018).
- [48] O. Gerberding, Deep frequency modulation interferometry, *Opt. Express* **23**, 14753 (2015).
- [49] K.-S. Isleif, O. Gerberding, T. S. Schwarze, M. Mehmet, G. Heinzel, and F. G. Cervantes, Experimental demonstration of deep frequency modulation interferometry, *Opt. Express* **24**, 1676 (2016).
- [50] L. Instruments, Liquid instruments, <https://www.liquidinstruments.com>.
- [51] M. Dovale Álvarez, *Optical Cavities for Optical Atomic Clocks, Atom Interferometry and Gravitational-Wave Detection* (Springer International Publishing, 2019).
- [52] J. Sanjuan, N. Gürlebeck, and C. Braxmaier, Mathematical model of thermal shields for long-term stability optical resonators, *Opt. Express* **23**, 17892 (2015).
- [53] M. Tröbs and G. Heinzel, Improved spectrum estimation from digitized time series on a logarithmic frequency axis, *Measurement* **39**, 120 (2006).
- [54] W. Riley and D. Howe, Handbook of Frequency Stability Analysis, Special Publication (NIST SP - 1065) (2008).
- [55] J. Gray and D. Allan, in *28th Annual Symposium on Frequency Control* (IEEE, Atlantic City, NJ, USA, 1974).
- [56] E. Rubiola, *Phase Noise and Frequency Stability in Oscillators* (Cambridge University Press, 2008).
- [57] J. Watchi, S. Cooper, B. Ding, C. M. Mow-Lowry, and C. Collette, Contributed review: A review of compact interferometers, *Rev. Sci. Instrum.* **89**, 121501 (2018).
- [58] J. Luo, L.-S. Chen, H.-Z. Duan, Y.-G. Gong, S. Hu, J. Ji, Q. Liu, J. Mei, V. Milyukov, M. Sazhin, C.-G. Shao, V. T. Toth, H.-B. Tu, Y. Wang, Y. Wang, H.-C. Yeh, M.-S. Zhan, Y. Zhang, V. Zharov, and Z.-B. Zhou, TianQin: A space-borne gravitational wave detector, *Classical Quantum Gravity* **33**, 035010 (2016).
- [59] Z. Luo, Z. Guo, G. Jin, Y. Wu, and W. Hu, A brief analysis to Taiji: Science and technology, *Results Phys.* **16**, 102918 (2020).